

A High-Resolution Characterization Of The Oxide-Metal Interface In Zircaloy-4 And Its Relation To The Oxidation And Hydrogen Pickup Mechanisms

James Sayers^a, Sergio Lozano-Perez^{a*1}, Rebecca J. Nicholls^a and Susan Ortner^b

^a Department of Materials, University of Oxford, Parks Road, Oxford OX1 3PH

^b National Nuclear Laboratory, Culham Science Centre, Abingdon, Oxon OX14 3DB

¹ Corresponding author.
e-mail address: sergio.lozano-perez@materials.ox.ac.uk

Abstract

Oxide growth and hydrogen pickup have been measured for Zircaloy-4 in environments of different pH. The metal-oxide interface has been studied at high-resolution over sufficient lengths to show meaningful trends in the behaviour of the ZrO and oxygen-saturated metal layers (suboxides). It was found that suboxide width decreases rapidly at transition, then increases more slowly. The suboxide width is a constant proportion of the dioxide width prior to transition, but drops then increases after transition. Density functional theory was used to predict suboxide stability under different pressures.

The behaviour of the suboxide can be explained on the assumption that the dioxide layer is the protective layer until it is bypassed by the environment percolating into the crack network.

The relation between hydrogen pickup rate and the oxide behaviour suggests that hydrogen moves across the Zircaloy-4 oxide with no net charge, and that the role of the constrained environment within the cracked fossil oxide requires investigation.

Key Words

Oxidation, Zircaloy-4, Suboxide, Interface, STEM, EELS, DFT

Highlights

1. Metal-oxide interface has been characterized analytically with nm-resolution over tens of microns.
2. Suboxide width decreases rapidly at transition, then increases more slowly.
3. Zirconium dioxide remains protective until it is bypassed by the environment percolating into the crack network.
4. Hydrogen appears to move across the Zircaloy-4 oxide with no net charge.

1. Introduction

Zirconium alloys are used for structural components in the fuel assemblies of water-cooled nuclear reactors due to their neutron transparency and their ability to withstand corrosion at high temperatures and maintain integrity under irradiation [1]. The precise alloy compositions and their processing routes have been modified continuously since their introduction in the late 1940s to reduce further their corrosion rates in primary water, to minimise the associated pickup of hydrogen and to reduce radiation-induced dimensional changes [2] [3] [4]. Oxidation and hydrogen pickup have been found to be complex processes so, although mechanistic understanding would help to focus alloy development and aid in the prediction of operational behaviour, developing that understanding has been slow. In recent years, detailed information from a variety of modern analytical and modelling techniques has improved the characterisation of the oxidation process, assisting the development of this mechanistic understanding. This work uses electron energy loss spectroscopy within a scanning transmission electron microscope (STEM/EELS) to characterise the progressive changes at the metal-oxide interface as a function of oxide thickness and oxidising environment in Zircaloy-4 and employs density functional theory (DFT) calculations to help interpret the observations. The trends observed support the development of an explanation of the cyclic nature of Zircaloy corrosion. The relation between the oxide, the interfacial region and hydrogen absorption in the samples also provides insight into the mechanism of hydrogen pickup.

1.1 Oxidation Of Zr Alloys

The oxidation of Zr and its alloys is a cyclic process. The initial oxidation rate follows a power law dependence on time (thickness= At^n ; A, n=constants, t=time), with an exponent, n, between 0.25-0.5 depending on the alloy, temperature and environment. For Zircaloy-2 and Zircaloy-4 in Light Water Reactor (LWR) coolants at operational temperatures, n is around 0.3 [5] [6] [7]. In this initial regime, the oxide appears generally protective. After a certain thickness (2-2.5 μ m in Zircaloys), the oxide becomes unprotective, the oxidation rate increases rapidly and a new period of power law growth initiates. The transition to higher growth rates does not happen at precisely the same time over the entire surface, and takes days or even weeks to complete. As the numbers of transitions between cycles increases, different parts of the surface fall further out of phase with each other and the overall oxidation rate appears linear [8]. At longer times still, the linear rate accelerates ("breakaway").

Many aspects of the oxide structure cycle with the growth rate. In the early part of each cycle (rapid growth), the oxide grains tend to be smaller and equiaxed, there is a higher fraction of tetragonal

ZrO₂, much fine intergranular cracking, and a flat metal-oxide interface [5] [9] [10]. In the mid-part of the cycle, the oxide grains tend to be columnar, the metal-oxide interface develops undulations, and in-plane cracks, running across several oxide grains, form behind delays in the oxidation front [5] [7] [11] [12]. At the end of the cycle, the in-plane cracks have formed interconnected rafts close to the metal-oxide interface [13], which can fill with water when they link to the surface via through-plane cracks [6] [14], even if these are widely-separated [15]. With the environment brought close to the interface again, the oxidation rate can increase. The faster growth rate can explain why the oxide grain size diminishes again at the beginning of the new cycle; the smaller grain size can explain the increase in tetragonal content, but the flattening of the metal-oxide interface at transition [13] [16] [17] is less easily explained. It is the flattening of the interface which suppresses in-plane crack formation after transition, giving the oxide its characteristic layered appearance in the optical and scanning electron microscope. The absence of these cracks also suppresses stress-relief, allowing the compressive stresses in the oxide to increase after transition [18]. It is within this, general, cyclic framework that the detailed mechanism must be understood.

At the atomic level, the oxidation of Zr and its alloys occurs via the inward diffusion of oxygen, with the matrix progressing towards the stable monoclinic ZrO₂ phase in stages. At low levels of oxygen, the O atoms distribute randomly on octahedral interstitial sites inducing expansions in both the c and a axes; once the O concentration approaches 25at.%, the O atoms begin to order, with a fully ordered distribution associated with the composition Zr₃O and a decrease in the a axis. Additional O atoms are then distributed randomly up to a solubility limit of 28.6 at.% [19]. In room temperature exposures to low partial pressures of O₂, Zr takes on progressively higher oxidation states (Zr⁺, Zr²⁺, Zr³⁺, Zr⁴⁺) with increasing O above the Zr solubility limit [20] [21]. In high temperature water (pure water or water with additions characteristic of operational LWRs), observations have been made of Zr₃O in Zircaloy-4, ZIRLO and Zr-2.5Nb using atom probe tomography (APT) [22] [23], selected area diffraction (SAD) in the transmission electron microscope (TEM) [24] and synchrotron X-ray diffraction (SXRD) [9]; and of ZrO (both sub-stoichiometric and super-stoichiometric) in Zircaloy-4, ZIRLO, Zr and Zr-0.4Fe-0.2Cr using APT [22] [23] [25] [24], in ZIRLO and Zr-1Nb using Electron Energy Loss Spectroscopy in association with scanning TEM (STEM/EELS) [26] [27] or Transmission Kikuchi Diffraction (TKD) [28], and with TEM/EELS [24]. Zr₃O has also been observed at higher temperatures in a range of materials and environments [29] [30] [31]. The widespread nature of these observations indicates that the oxidation of Zr alloys at elevated temperature also proceeds via a sequence of oxidation states, even though the Zr⁺ and Zr³⁺ states are no longer readily found.

When the same material is observed after different exposure times, it appears probable that the lower stoichiometry oxides thicken up to transition. The lower stoichiometry oxides are, however,

of variable thickness along the oxidation front, so it is difficult to show the development of the suboxide region as a function of overall oxide thickness, alloy composition or environment without an intensive investigation covering reasonable lengths of the oxidation front and multiple oxidation times [27] while preserving nm analytical resolution. This paper presents such a study on Zircaloy-4 exposed to two different oxidation environments. The first environment is pure water at 360°C and the second is replica PWR water with KOH added to increase the environmental pH (i.e. reduce the proton availability in the environment) and, hence, to reduce the hydrogen pickup rate [32] in order to observe any correlations between the substrate oxidation process and hydrogen pickup. KOH was chosen to modify the pH rather than increasing the LiOH content as KOH has been found to affect the oxidation process less than LiOH [33]. The pure water testing was part of a broader programme, MUZIC 2, which focused on the mechanisms controlling oxidation and H pickup in Zr alloys [34, 27].

The pH itself has been reported to have no effect on the oxidation rate, unless it is extremely low or extremely high (below 1 or above 13) [6]. It does, however, affect the hydrogen pickup fraction as described in an interim report on this project [32]. Using the two different environments is intended to clarify whether the suboxide interacts with the hydrogen pickup process.

2. Experimental

Zircaloy-4 sheet (Zr-1.31Sn-0.20Fe-0.11Cr-0.13O % by weight, 9 wt. ppm H) was provided by Westinghouse. Corrosion coupons 25 mm x 70 mm x 0.5 mm were exposed in a static autoclave at Amec Foster Wheeler (now Wood plc). The corrosion environment was 50% heavy water, containing 2 wt. ppm Li, 95 wt. ppm wt. K and 1050 wt. ppm B at 350°C ($\text{pH}_{350} = 8.82$). The autoclave was emptied and refreshed and the samples weighed every 5-30 days. The weight gains were compared to those of samples exposed to pure water at 360°C ($\text{pH}_{360} = 6.15$) by Westinghouse Electric Company. The weight gains were converted to average oxide thicknesses using a conversion factor of $15\mu\text{g}/\text{dm}^2 = 1\mu\text{m}$ [5].

The hydrogen content of the samples was monitored using the total counts associated with hydrogen and deuterium when 10mm x 10mm x 0.5mm samples were heated to 800°C in a Hiden Analytical TPD (Thermal Programmed Desorption) workstation. The oxides were not removed prior to TPD analysis. The counts were normalised to wt. ppm using calibrated measurements provided by the Paul Scherrer Institute and Westinghouse performed with Hydrogen Hot Gas Extraction on a selection of samples [35].

Samples were prepared for STEM/EELS with the focussed ion beam miller (FIB) in-situ lift-out method [36] [37] [38] using a FEI FIB200 for initial lift-out and a Zeiss NVision FIB-SEM or a Zeiss

Crossbeam 540 for thinning to electron transparency. STEM and EELS were carried out on a cold field emission source JEOL ARM-200F, with an acceleration voltage of 200kV. High-angle annular dark field (HAADF) images were obtained with two JEOL ADF detectors (located before the viewing screen) and a Gatan ADF (located just before the EELS spectrometer). EELS data were acquired with a Gatan Quantum GIF spectrometer, using dispersions of 0.25 and 0.05eV/channel. The convergence and collection half-angles were 31 and 41 mrad, respectively.

A set of reference low-loss EELS spectra were produced by identifying features of interest in the metal and oxides and acquiring spectra from pixels within those features. The features of interest are identified in Figure 1. They were the Zr metal, zirconia (ZrO_2), ZrO, an oxygen-saturated zirconium (OSZ) region, zirconium hydrides, and second phase particles (SPPs). (The red box shows the location at which the illustrated reference spectrum for zirconia was acquired.) All the reference spectra are shown in Figure 2. Spectrum images (SIs) were acquired at the metal-oxide interface and the spectrum at each pixel was fitted to a combination of the reference spectra using the Multiple Linear Least-Squares (MLLS) technique [39, 40]. This enabled nm-resolution phase mapping of the distribution of the different components around the oxide-metal (OM) interface, as shown in Figure 3 to be performed in around ~5 mins. MLLS was carried using the analysis software Digital Micrograph (DM) made by Gatan Inc. It should be noted that the reference spectra used for the MLLS fitting do not always fully reproduce the experimental spectrum. In particular, bad reconstructions appear near cracks due to changes in plasmon shapes near surfaces and some components appear with positive signal in regions where they are not expected. Nevertheless, the trends and phases are clearly identified and the required phase thickness measurements achieved successfully.

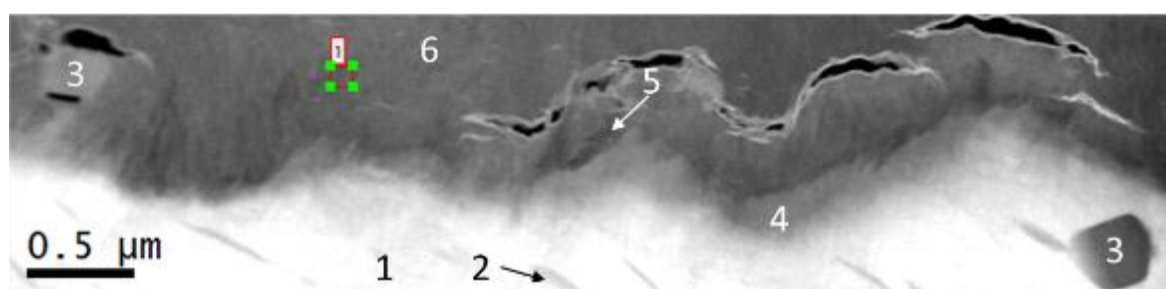


Figure 1 – HAADF image showing the oxide-metal interface region on sample exposed to $\text{pH}_{350}=8.82$ for 91 days ($1.83\mu\text{m}$). The numbers indicate the location of the extracted reference spectra in Figure 2. The labelled regions are: 1 – Metal, 2 – Hydride, 3 – SPP (one in the oxide and one in the metal), 4 – Oxygen Saturated Zirconium (OSZ), 5 – ZrO, 6 – Oxide. The box shows the size of the area used to extract the reference spectra ($\sim 100 \times 100 \text{nm}$)

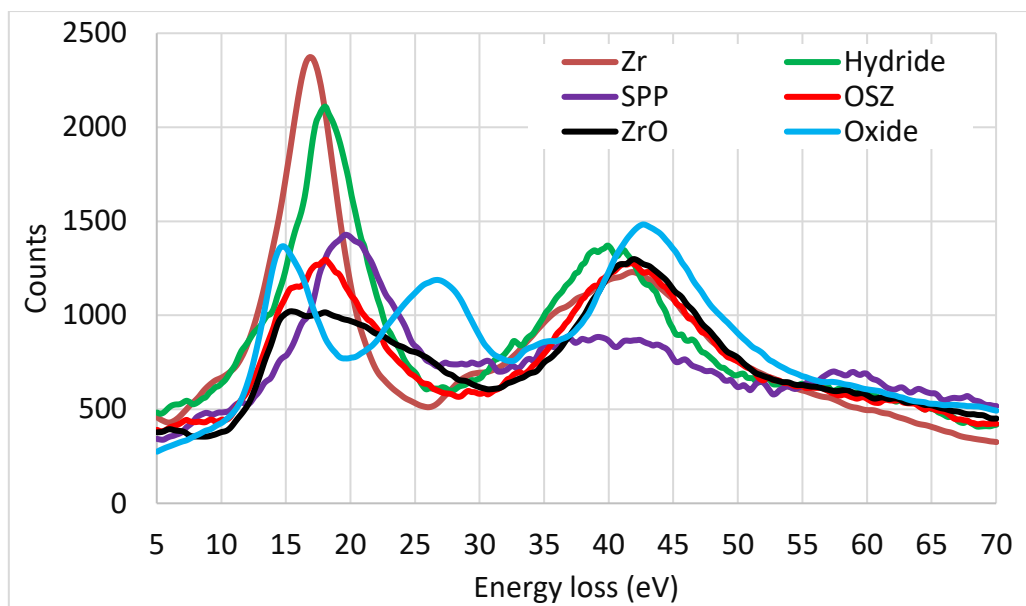


Figure 2 – EELS spectra showing the plasmon peaks for the different regions labelled in Figure 1.

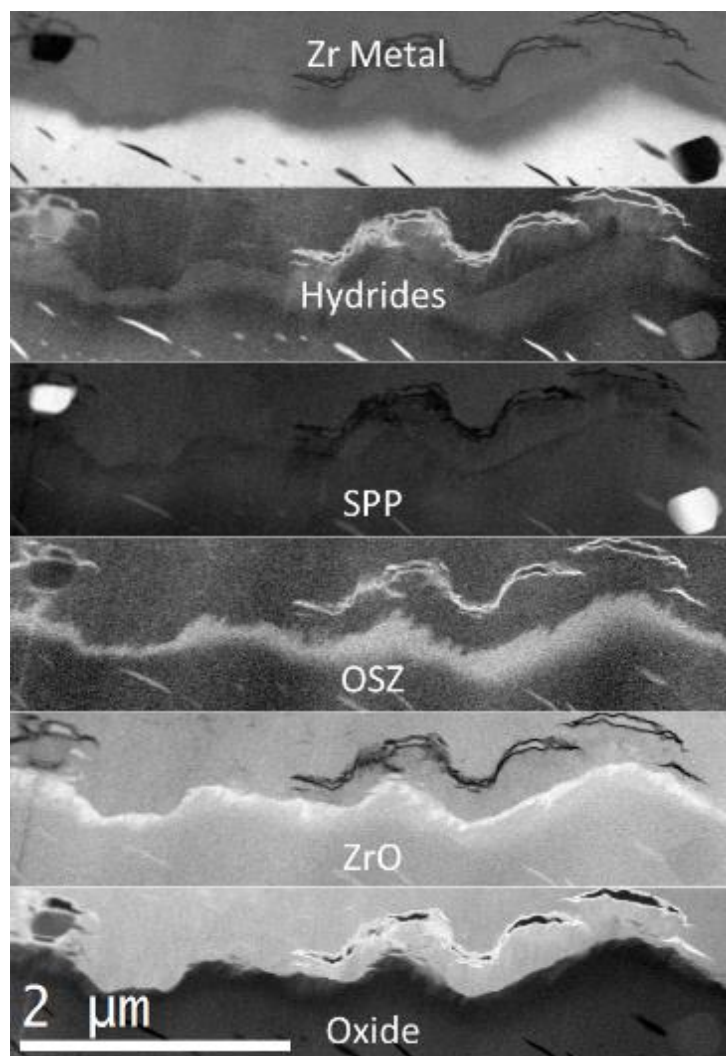


Figure 3 – MLLS fit for the 6 regions in Figure 1 From top to bottom: Metal, Hydrides, SPPs, OSZ, ZrO, and Oxide. Lighter areas show the strongest match to the input spectrum.

The thicknesses of the OSZ and ZrO regions were computed from their respective phase maps after segmentation with Mercury Software's Avizo. An example of the segmented binary image for the OSZ map in Figure 3 is shown in Figure 4. The phase thickness was calculated by projecting the segmented map vertically (along the oxide growth direction), turning it into a 1D image where every pixel has a value equal to the phase thickness at that point. Representative means and standard deviations were then derived for the OSZ and ZrO layers in each sample.



Figure 4 – Segmented OSZ map (now a binary image)

3. Calculations

The effect of stress on the relative stabilities of ZrO_2 , ZrO and Zr_3O was examined using first principles calculations. Pseudopotential density functional theory (DFT) code CASTEP [41] was used to calculate the formation enthalpies of the three phases at hydrostatic pressures between -3 and +3 GPa. (Note: we have used the engineering convention in which a compressive stress, sometimes viewed as a positive external pressure, is defined as a negative hydrostatic stress.) Calculations were carried out with ultrasoft pseudopotentials and a PBE exchange correlation potential. An energy cut-off of 490eV and k-point sampling of at least $2\pi \times 0.03 \text{ \AA}^{-1}$ was used for all calculations. For each pressure the structure was optimised until the forces on each atom were less than $1 \times 10^{-3} \text{ eV/\AA}$.

A convex hull was constructed at each pressure and the position of the ZrO phase with respect to the line joining ZrO_2 and Zr_3O was used as an indication of the stability of the ZrO (i.e. if the formation enthalpy of the ZrO phase falls below the line joining the ZrO_2 and Zr_3O phases, then ZrO is considered stable).

4. Results.

Figure 5 shows the oxide growth computed from the weight gain data. For both environments, the oxide thickness at transition is approximately $2.2 \text{ }\mu\text{m}$. Transition progresses across the samples over a period centred around 100 days in pure water at 360°C and around 130 days elevated pH and 350°C .

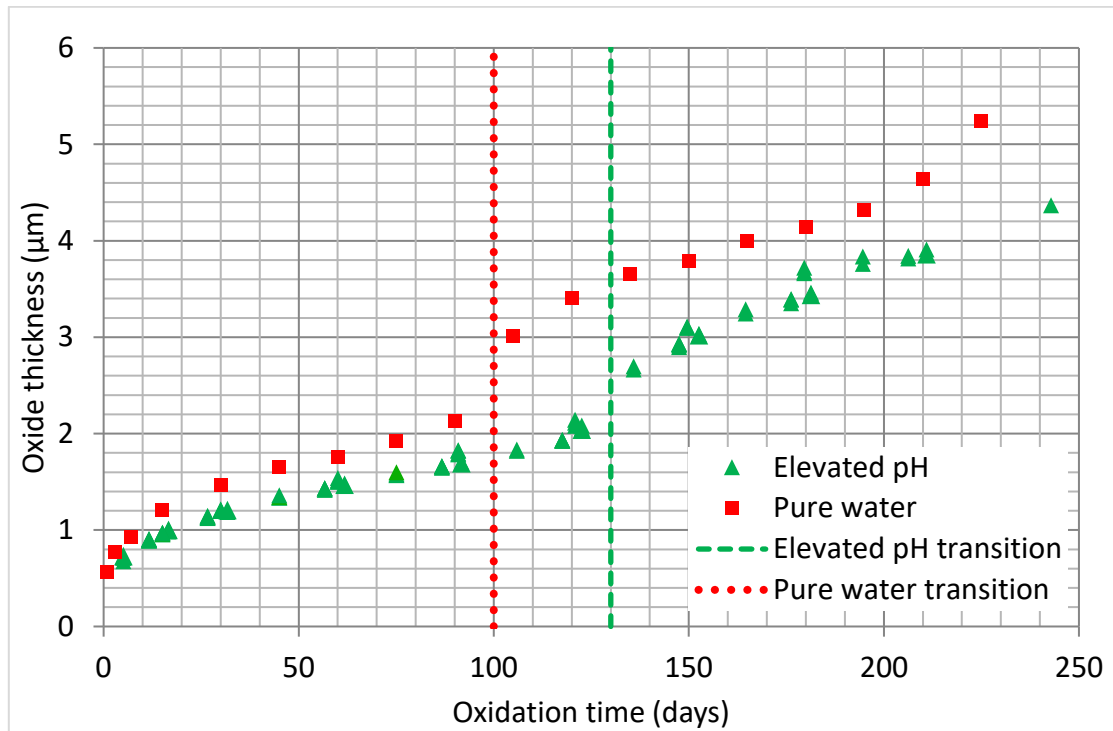


Figure 5 - Comparison of samples oxidized in pure water at 360°C vs samples oxidized in elevated pH at 350°C.

Figure 6 and Figure 7 show the OSZ and ZrO phase maps at the OM interface of a sample exposed for 15 days in the high pH environment (average oxide thickness = 0.96 μm). The OSZ is a continuous layer of varying thickness: In the upper images of the montage, the OSZ is thicker on facets of the interface which run from upper right to lower left; in the lower images, it appears thicker in the delays in the oxidation front than at the protuberances. The ZrO is discontinuous and, in some locations, shows a saw tooth morphology. It is equally likely to appear when the OSZ is thick or thin. Cracks in the oxide (ZrO_2) image with a bright rim in the OSZ map due to the edge effects mentioned in Section 2, but are not included in the assessment of OSZ thickness. The cracks are generally dark in the ZrO map. The dark elongated features in the metal substrate in the OSZ map are hydrides.

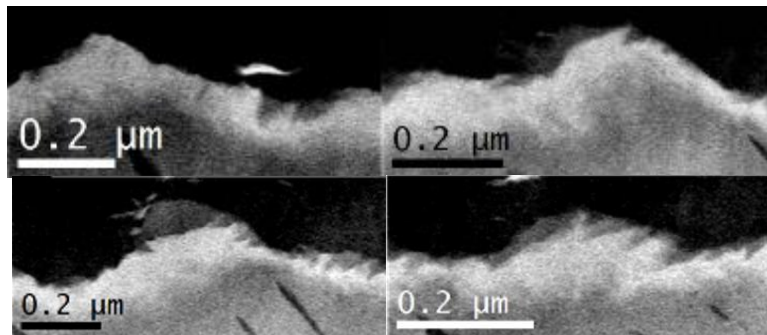


Figure 6 - OSZ map at OM interface in a sample exposed 15 days to high pH water (oxide thickness = $0.96\ \mu\text{m}$)

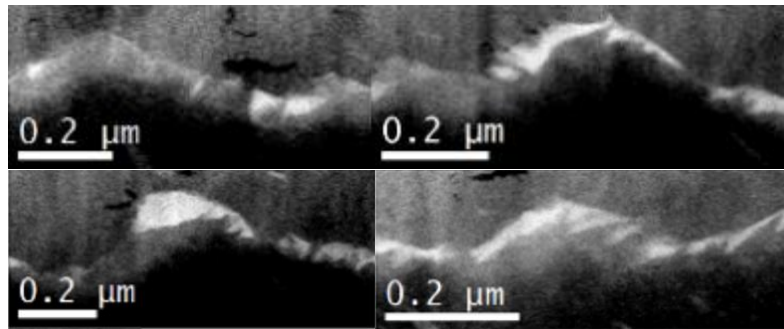


Figure 7 - ZrO map in region shown in Figure 6.

Figure 8 and Figure 9 show the OSZ and ZrO maps from the OM interface of a sample exposed 27 days in the high pH environment (average oxide thickness = $1.14\ \mu\text{m}$). There is no systematic variation of the OSZ thickness with protrusions / delays or local orientation along this interface. The ZrO is more continuous in this sample and exhibits the saw-tooth morphology throughout. More than one substrate grain is present in this montage, as evidenced by the changes in the hydride and saw-tooth orientations. In both grains the saw tooth axis is approximately normal to the hydride long axis.

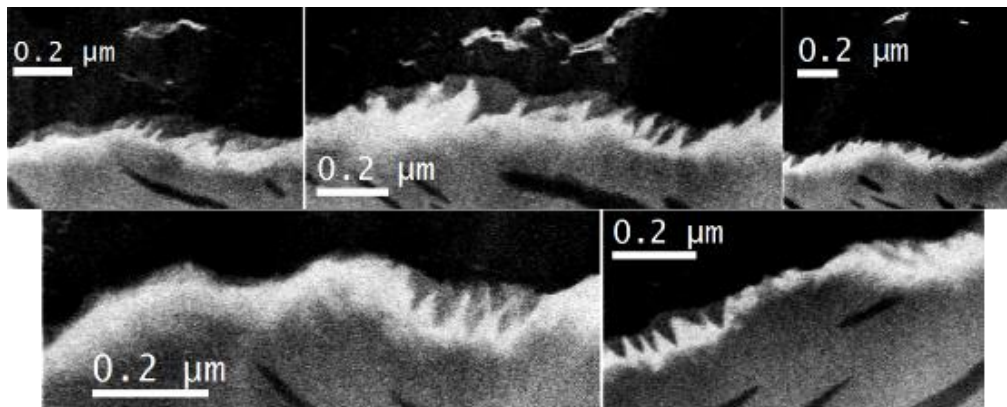


Figure 8 - OSZ map at OM interface in a sample exposed 27 days to high-pH water.

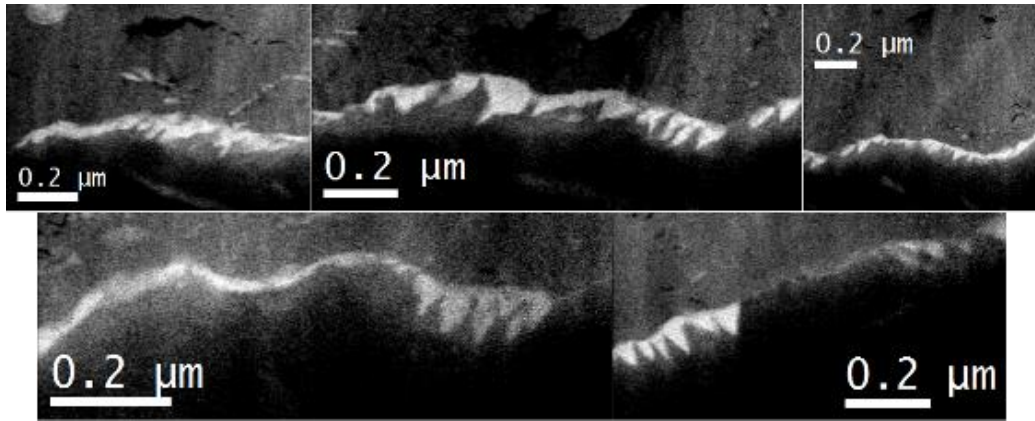


Figure 9 - ZrO map in region shown in Figure 8 .

The OSZ and ZrO maps at the OM interface of a sample exposed for a 62 days at high pH (average oxide thickness = $1.47\ \mu\text{m}$) are shown in Figure 10. There are a few large cracks in the oxide near delays in the oxidation front, with both the OSZ and ZrO being thicker within these delays. The ZrO is again serrated and aligned normal to the hydride direction. A patch of ZrO which appears to be surrounded by oxide (ZrO_2) and separated from the main ZrO and OSZ regions is marked with an arrow in Figure 10.

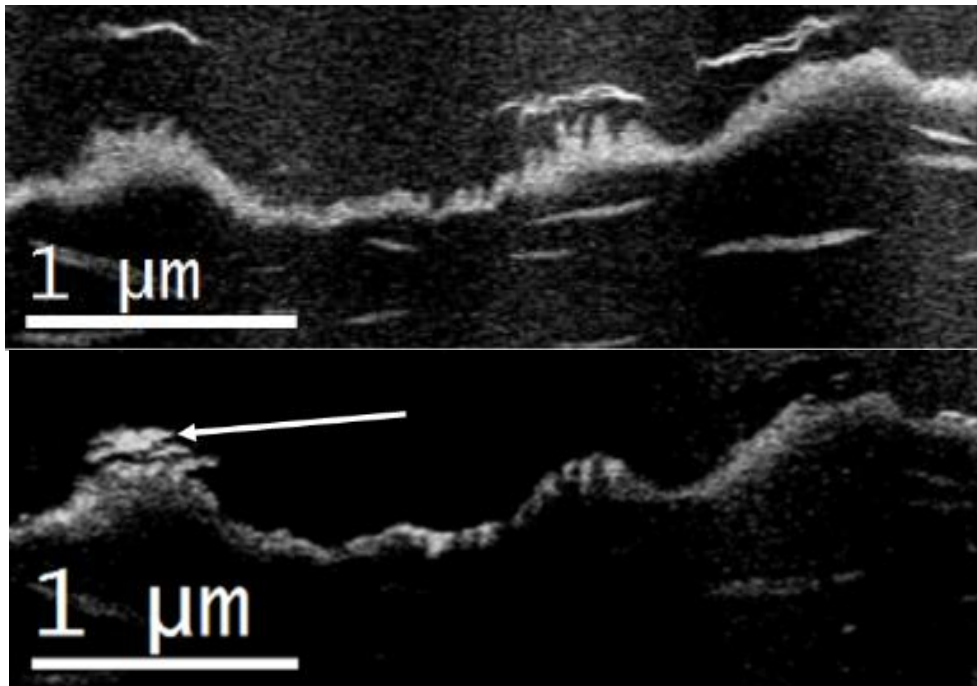


Figure 10 – (Top) OSZ map at OM interface in a sample exposed 62 days to high-pH water. (Bottom) ZrO map. The white arrow indicates a region of ZrO separated from the rest of the ZrO + OSZ region.

The OSZ and ZrO maps from the sample exposed 123 days to high pH (average oxide thickness = $2.06\ \mu\text{m}$) are shown in Figure 11. Some parts of the 123 day sample in this environment will have

gone through transition, but the crack distribution suggests that the region shown here has not. The ZrO layer here is much more continuous than in the previous maps.

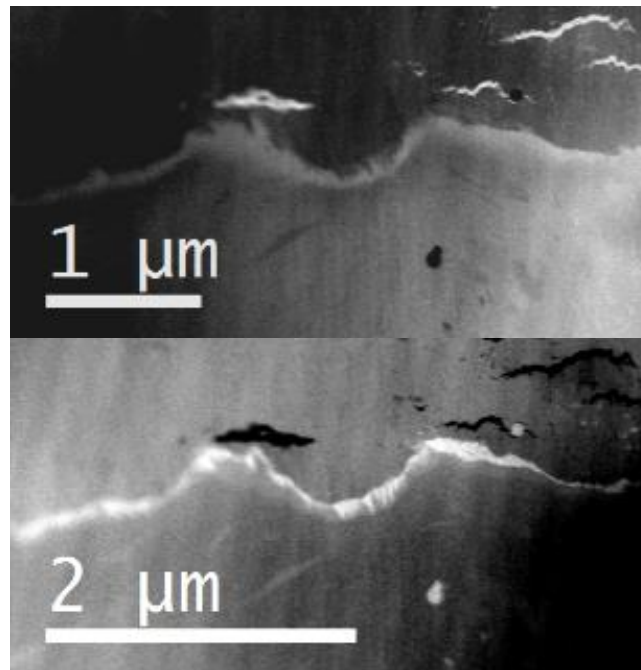


Figure 11 – (Top) OSZ map at OM interface of sample exposed 123 days in high-pH water. (Bottom) ZrO map.

Figure 12 shows maps from the post-transition 148 days high pH sample (average oxide thickness = $2.92\mu\text{m}$). There is very little ZrO at this stage of oxidation.

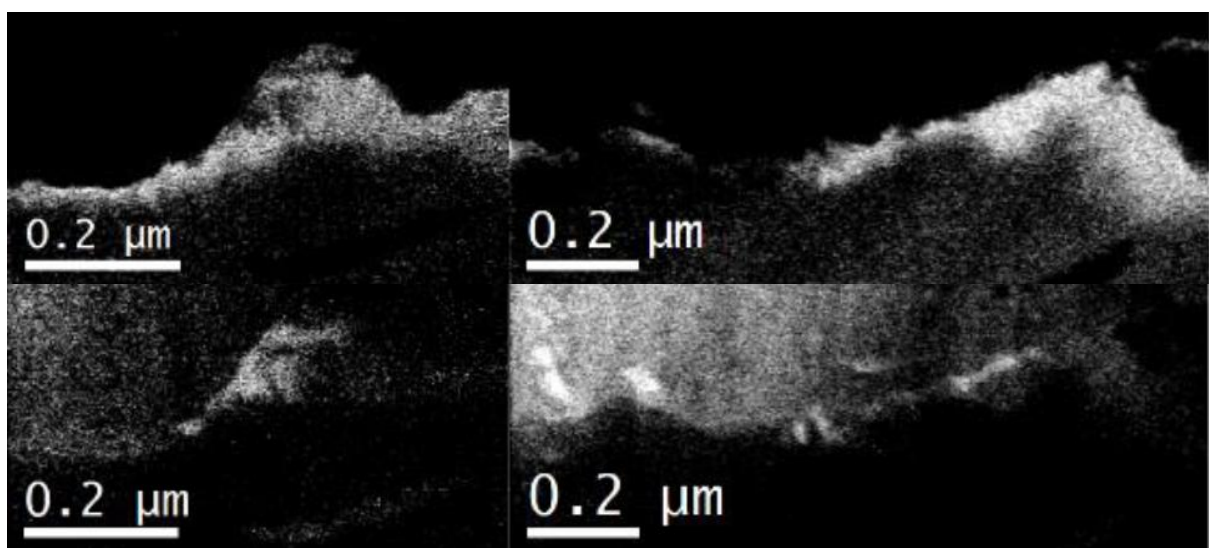


Figure 12 – (Top) OSZ maps at OM interface of sample exposed 148 days to high-pH water. (Bottom) ZrO map

Maps from a 211 days high pH sample (average thickness = $3.88\mu\text{m}$) are shown in Figure 13. Both layers have thickened and there are continuous regions in the ZrO. The white region in the metal in the right-hand image of Figure 13 is an SPP.

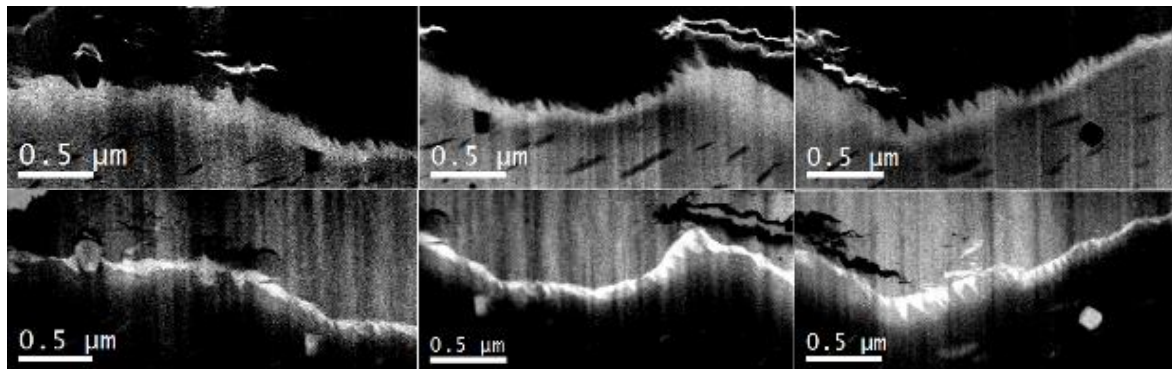


Figure 13 – (Top) OSZ maps at OM interface of sample exposed 211 days to high-pH water. (Bottom) ZrO maps

Figure 6 - Figure 13 show that the forward front of the OSZ appears smooth even when the ZrO behind it is very serrated and, hence, the OSZ width is very variable. Adding the OSZ and ZrO thicknesses shows the penetration of the OSZ front from the oxide into the metal. This total region will be referred to as the suboxide layer from now on.

Plots of the suboxide (ZrO+OSZ) layer as a function of oxide thickness are shown in Figure 14 for samples exposed in both pure water at 360°C and high pH water at 350°C . In Figure 14, the effect of the difference in temperature has been scoped by showing both the raw pure water data and the pure water data scaled by the ratio of the oxygen diffusion rates at 350°C and 360°C . The trends are not affected by the scaling. In both environments, the suboxide layer thickens towards transition and thins at transition. Both the OSZ and ZrO thicknesses fall considerably around transition. In both the first and second oxidation cycle, no ZrO was observed during the first micron of oxide growth.

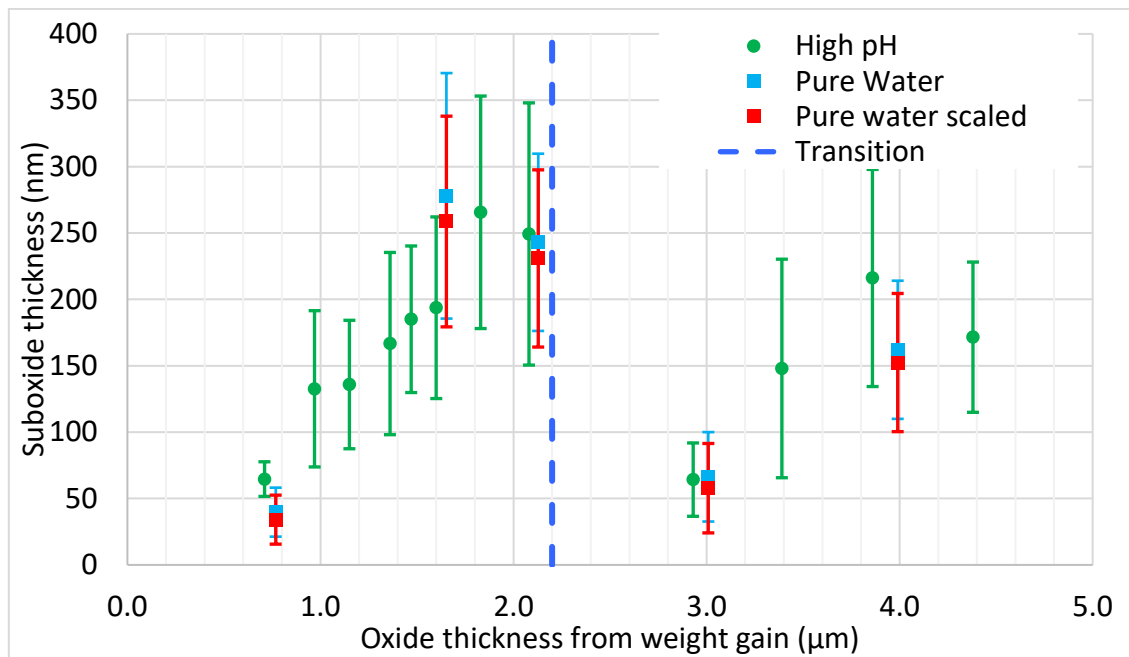


Figure 14 - Variation in the thicknesses of the OSZ + ZrO regions during oxidation in high pH water at 360°C and in pure water at 350°C. The error bars are the standard deviation of the data.

Figure 15 plots the thickness of the OSZ, ZrO and total suboxide layers as a function of the dioxide (ZrO_2) thickness and oxidation time. The high pH data show that the mean thicknesses of the ZrO, OSZ or (OSZ+ZrO) layers are each constant fractions of the ZrO_2 thickness throughout the pre-transition region (regardless of the instantaneous oxidation rate). Although the data for the pure water samples are more sparse and more scattered, the same may well hold in the second environment.

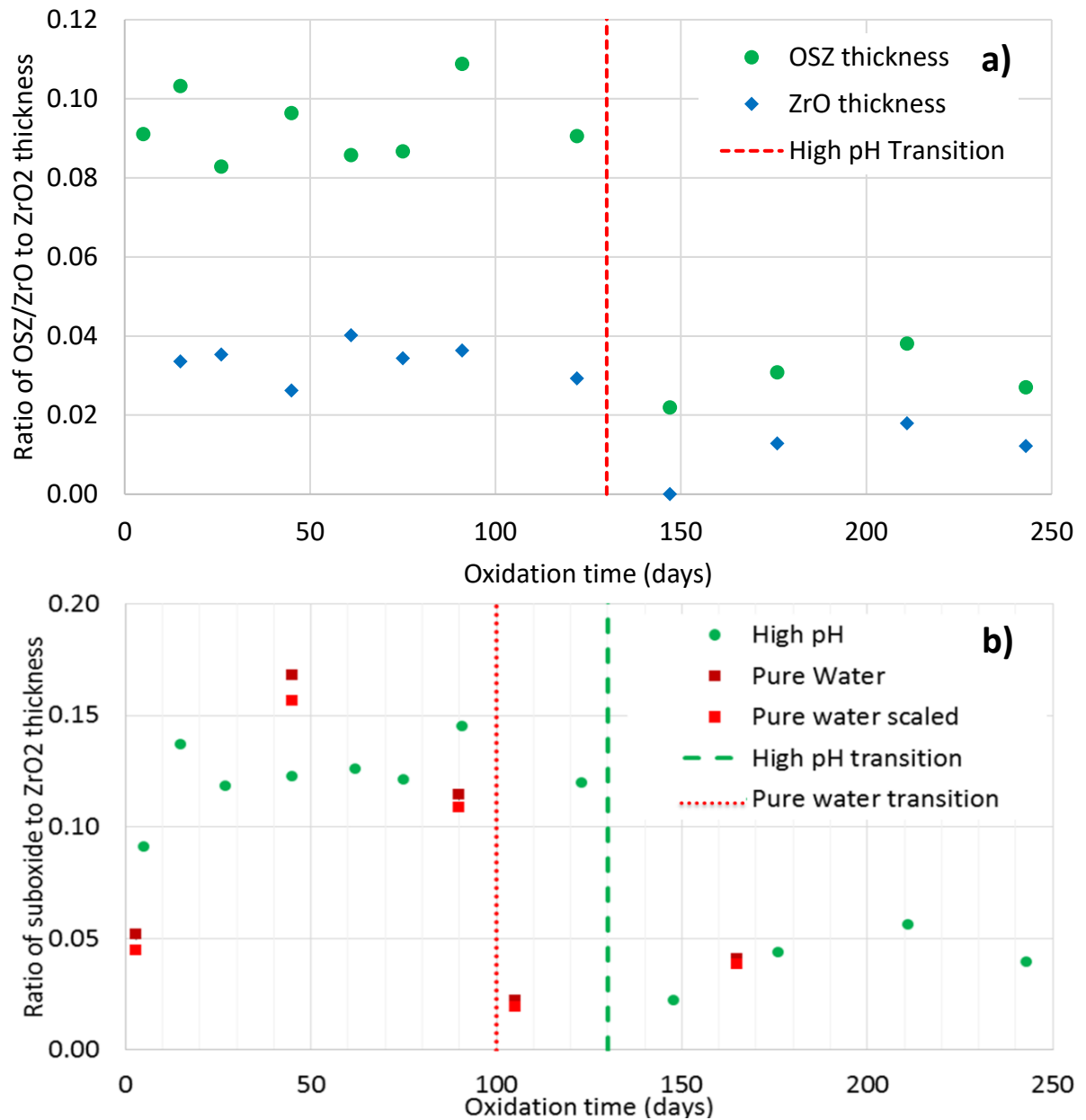


Figure 15 – Different intermediate layers as proportions of oxide thickness. (a) Ratio of ZrO and OSZ to ZrO₂ thickness in high pH. (b) Ratio of ZrO+OSZ to ZrO₂

The hydrogen contents of the samples (including all isotopes) are shown in Figure 16. There is an initial small increase in the hydrogen content after the samples are put into the autoclave. The hydrogen content then remains roughly constant until near the end of the first cycle, whereupon it begins to increase further. It is not clear from these data alone whether the hydrogen content levels off during the second cycle or increases continuously. In the light of the literature [42, 43], it is probable that the H content does not level off, but any increase is very slow in the high pH environment. The pH of the environment does not affect the hydrogen pickup in the first cycle but,

in the second cycle, around 5 times more hydrogen is picked up from the lower pH (high proton concentration) environment over a given increment in oxide thickness.

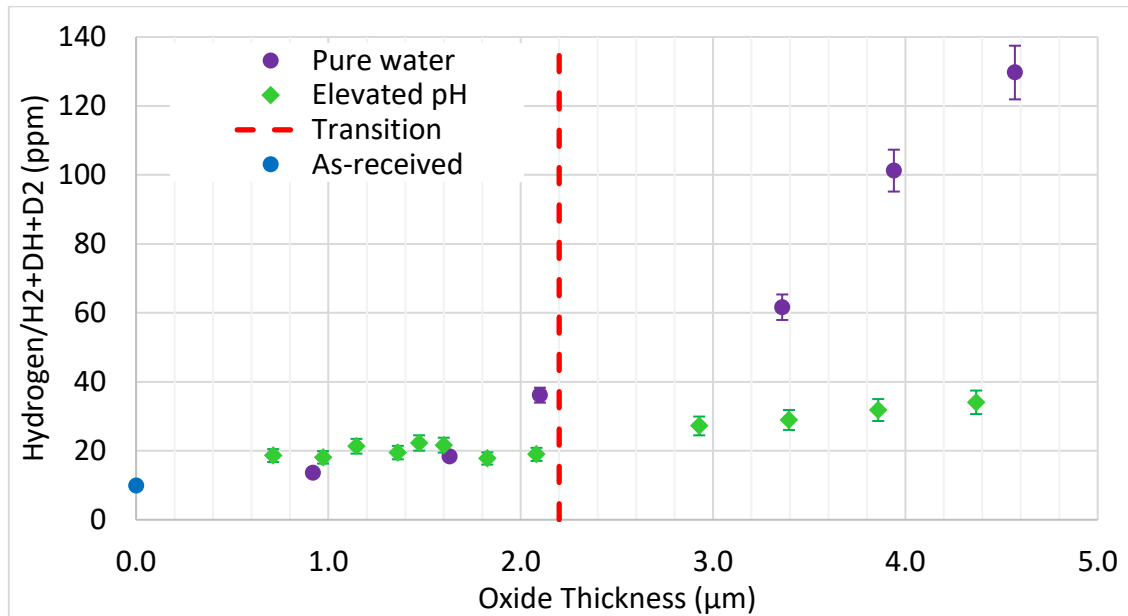


Figure 16. Comparison of hydrogen content (H_2) for samples oxidised in pure water and the combined $H_2 + DH + D_2$ for samples oxidised in a high pH (50% deuterated), against oxide thickness

The modelling of the stability of the OSZ and ZrO phases vs. applied stress revealed that a compressive stress stabilised the ZrO phase. The formation enthalpy for all the phases became less negative as the compressive stress was increased, but the effect of stress was most pronounced on ZrO_2 , followed by ZrO and Zr_3O (Figure 17). In consequence, the formation enthalpy for ZrO moved further below the convex hull (situation for 0GPa shown in Figure 18). In contrast, tension tended to destabilise ZrO (decreased the distance below the convex hull). Zr_3O and ZrO were, however, found to be thermodynamically stable at all pressures considered (-3 to 3 GPa pressure). All three phases are anisotropic, but it was found that applying different stresses/strains in different directions had little effect on the stability of the phases meaning that no dependency of stability on orientation was found by considering the stress alone. It should be noted that these calculations are for bulk materials, which might limit their applicability on the constrained thin layers that are relevant for the alloys considered in this study.

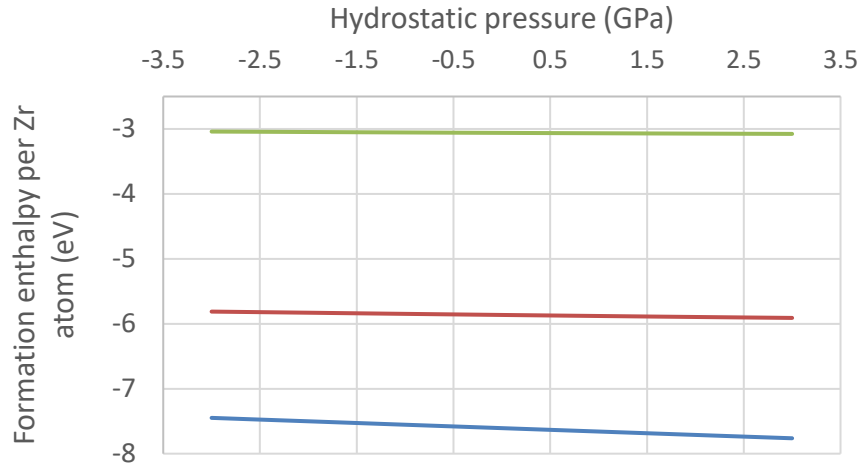


Figure 17. Variation in the formation enthalpy of the different phases with hydrostatic pressure.

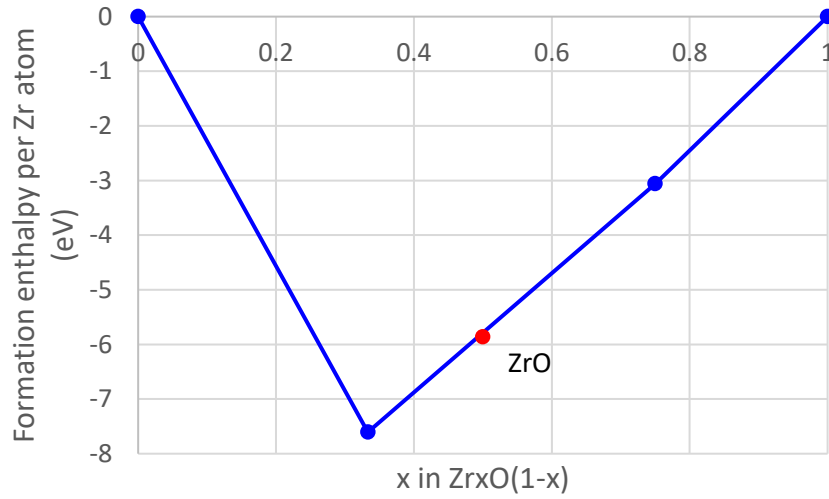


Figure 18. Convex hull for 0 GPa and the position of the formation enthalpy of ZrO

5. Discussion

5.1 Phase Thicknesses And Oxide Cycling

This study of the interface region has shown the detailed development of the suboxide over two oxidation cycles. The information can be used to clarify the significance of the suboxide at different stages in the oxidation process. It is clear that the OSZ and the mean thickness of the ZrO region both increase as the oxide thickens. This thickening of the OSZ and ZrO could relate to either the increase in dioxide thickness or the decrease in the instantaneous oxidation rate towards each transition.

Figure 15 shows that the ratio of the mean suboxide width to the mean dioxide thickness is a constant prior to transition, regardless of dioxide thickness. This indicates that the time dependence must be the same for the forward movements of both the mean suboxide: metal interface and the mean dioxide : suboxide interface i. e. if growth is described by a power law dependence on time, $\text{thickness} = A \cdot \text{time}^n$, where $A = \text{constant}$, the exponent, n must be the same for each interface ($n_{\text{sub}} = n_{\text{ZrO}_2}$). Since the suboxide : metal interface moves faster than the dioxide : suboxide interface, its movement can be described with a higher value of the coefficient A ($A_{\text{sub}} > A_{\text{ZrO}_2}$). (Note, these are merely empirical descriptions of the movements of the two oxidation fronts; it may be that, mechanistically, both should be described with logarithmic or some other functional dependences.) With the same value of n for both interfaces, but differing values of A , the widening of the ZrO and OSZ layers towards transition is a natural consequence of the extended oxidation time. Since widening would be observed regardless of whether n was greater or less than unity, the widening of the ZrO and OSZ layers does not appear to be a consequence of the reduction in the instantaneous growth rate of the dioxide with time.

In detail, there are variations about the mean rate of movement for both the suboxide to metal interface and the dioxide to suboxide interface: The dioxide shows grain-to-grain variations in thickness and shorter-scale undulations; in many places, the OSZ appears thicker within the delays in the ZrO_2 front than ahead of the protuberances; the ZrO begins in a discontinuous fashion with individual grains along the oxidation front, (in agreement with [22] [28] [28] [44]) which grow and link to form a more continuous layer prior to transition. These ZrO grains exhibit an orientation effect in that they have the saw-tooth appearance characteristic of Widmanstätten precipitation, tend to be larger on one side of a protuberance than another and align with respect to the hydrides in the metal substrate. The saw-teeth rarely form at the ends of the protuberances. As a result, the mean ZrO content is also greater in the delays.

The frequently greater thickness of the suboxide layer (OSZ + ZrO) within the delays in the oxidation front could reflect the local stress redistributions around the interfacial undulations, a relation between the suboxide thickness and cracks in the dioxide layer or an observational bias. Considering first the stress effects, while the interface is flat the oxide is uniformly in in-plane biaxial compression and the underlying metal very slightly in tension, but the metal within the delays becomes more triaxially tensile as the undulations increase in amplitude [45] (i.e. the hydrostatic pressure becomes more negative). The DFT calculations performed here predict that an increase in tensile stress would, if anything, tend to destabilise the ZrO with respect to the ZrO₂ within the delays. Thus the higher suboxide content within the delays appears to be an effect of the local kinetics rather than the result of the changing phase stability. Possible kinetic effects include an increase in the diffusion rate of O in Zr under tension, encouraging the removal of O from the OSZ-dioxide interface and a reduction in the rate of supply of O to the OSZ-dioxide interface beneath in-plane cracks.

The next question to consider is whether (i) the suboxide is protective and, hence, its loss at a certain oxide thickness induces transition or (ii) another part of the oxide is protective and the loss of the suboxide is a consequence of transition. The amplitudes of the interfacial undulations increase as the dioxide thickens and this could, in the extreme, produce a sufficient local tensile stress that the ZrO is completely destabilised with respect to Zr₃O and ZrO₂. If the ZrO constituted the protective layer in the oxide, this could then trigger the increased oxidation rates associated with transition. Comparing the magnitude and distribution of the stresses expected within delays of the amplitude observed experimentally [45] with the calculations showing that the ZrO will be stable within at least -3GPa - +3GPa, however, leads to the conclusion that the ZrO layer is only likely to be lost at the base of a delay in the oxidation front. If protectivity is lost first at this point, then the consequent local increase in the dioxide growth rate would make the undulation more shallow, reducing the local tensile stress and restabilising the ZrO. Thus, if the ZrO were the protective layer, destabilised by the change in stress as the undulations increase in amplitude, this would induce a steady state undulation amplitude. An approach to a steady state amplitude may have been observed in a Sn-free ZIRLO-type alloy, but not in ZIRLO or Zircaloy-4 in the same study [17]. Thus the stress-induced modification of a protective ZrO layer might, possibly, occur in Sn-free ZIRLO, but not in ZIRLO or Zircaloy-4, and would not induce transition in any of these systems. A dominant influence of undulation-induced stresses on the behaviour of the ZrO would also not explain why Zr₃O or OSZ disappeared at the same time as the ZrO.

If the loss of the suboxide is to be understood as a consequence rather than a cause of transition, it is necessary to consider the sequence of events around transition. At transition, through-thickness

cracks bring the water into the network of in-plane cracks which reaches to the oxide-suboxide interface. The through-thickness cracks are induced by heterogeneity in the strains in the metal substrate [46]. The in-plane crack network is extensively interlinked [13] [46], so very few through-plane cracks are required to bring water close to the dioxide : suboxide interface over a wide area. Since the in-plane crack network initiates behind delays in the oxidation front, the delays represent the new forward limit reached by the water. At the instant water fills the lateral crack network, the environment is extremely close to the metal-oxide interface at the delays, so the oxidation rate at the delays becomes extremely high just after transition. At the protrusions, however, the environment is separated from the oxidation front by the protrusion amplitude (0.3-0.5 μm near transition), so the immediate post-transition growth rate here is lower than at the delays (although still high). These different growth rates act to smooth out the undulations in the oxidation front after transition. Without delays in the oxidation front, the local out-of-plane tensile stresses are lost [45], new in-plane cracks do not form in the dioxide and the in-plane crack network is truncated. Even if through-plane cracking were retained at this stage, it would no longer be associated with the supply of water to large areas of the interface because of the cessation of the in-plane crack network. In consequence, the high oxidation rates cannot be maintained, and the post-transition oxide becomes protective until the undulations reform and a new network of in-plane cracks can develop and link to the surface. Within this mechanical description of transition, it is not necessary for the suboxide layer to play a role in either the increase in the growth rate or the consequent flattening of the interface which produces the subsequent decrease in growth. This mechanical model of transition can, however rationalise the reduction in thickness of the suboxide layer as a consequence of transition, as discussed below.

When water fills the crack network within the dioxide, the effective distance from the water to the suboxide front will (although small) be significantly greater than that from the water to the dioxide front. Immediately upon transition, then, the dioxide is effectively at an earlier stage in the thickness versus time curve than the suboxide layer. The rates of movement of both interfaces increase, but the dioxide growth rate is temporarily faster than the suboxide layer growth rate. As both regions extend, the difference in widths becomes less significant, and the effect of the larger A value for the suboxide begins to dominate again. The results of a simplistic calculation showing the effect of the different changes in thickness at transition (for the case of a dioxide thickness falling to zero at transition) is shown in Figure 19.

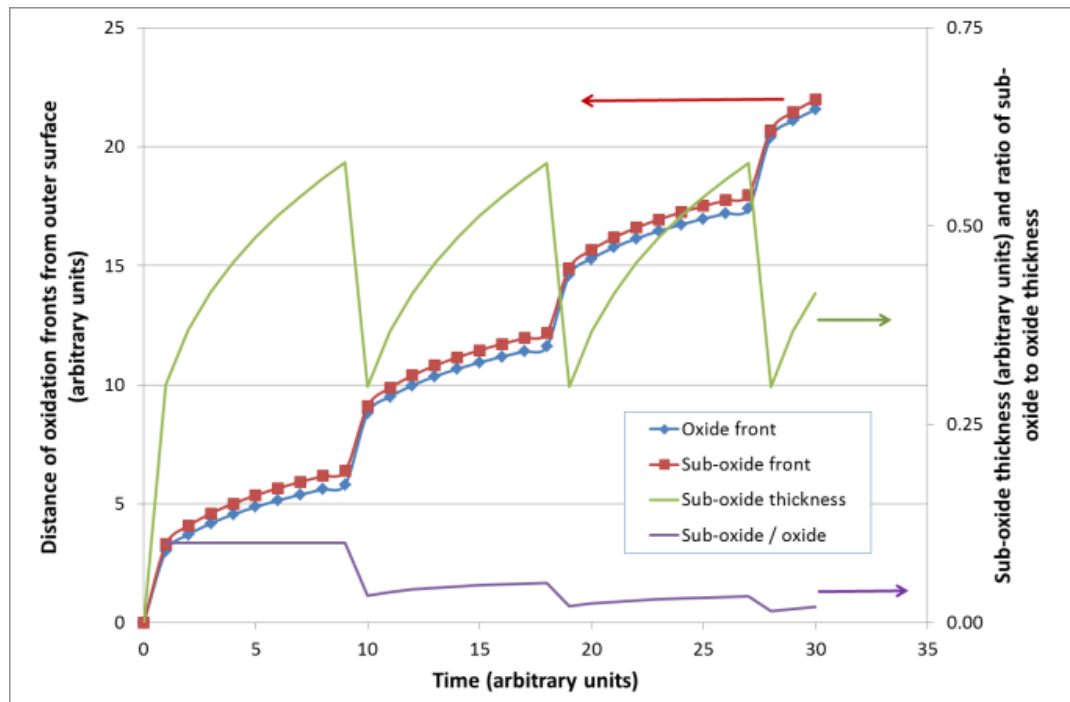


Figure 19. Position of interfaces of oxide and suboxide, width of suboxide layer and ratio of suboxide width to oxide thickness when both interfaces move according to distance= At^n with $A_{\text{suboxide}}=1.1 \cdot A_{\text{oxide}}$, $n=0.3$, and the effective oxide thickness falls to zero at transition (arbitrary units for the purpose of qualitative comparison).

The calculation reproduces the essential features of the data: a constant ratio between suboxide and dioxide before transition; a lower but increasing ratio after transition; widening of the suboxide up to transition; reduction in suboxide width around transition. It is thus plausible that the change in the thickness of the suboxide is a consequence of the loss of protectiveness of the dioxide layer at transition, rather than transition being a consequence of the loss of the suboxide layer.

5.2 Effect of pH

The two environments examined here differ in their solute content (B, K, Li) and, hence, pH and they induce different hydrogen pickup rates. The intention behind the use of the high-B-Li-K environment was to reduce the hydrogen pickup rate by reducing the proton availability at the oxide surface. The hydrogen pickup rate was, indeed, lower in the high-pH environment but it is worth noting that solute effects could have also influenced the hydrogen pickup rates achieved, as increasing the solute content or Li/B ratio can either increase or decrease the HPF [47].

Regardless of the precise cause of the change in hydrogen pickup rates, the relationship between the pH, the details of the oxidation process and the hydrogen pickup provides some insight into the mechanism of hydrogen pickup. In his reviews, Cox [5] [6] concluded that moderate changes in pH did not affect oxidation rates. In this context, both the chemistry and pH changes were sufficiently

small that the difference in oxidations rates in the two environments was expected to relate only to the difference in temperature. The pretransition growth data can be fitted by power law expressions:

$$y_{pH} = 0.42t^{0.31} \quad y_{pw} = 0.53t^{0.31} \quad (1)$$

Where y_{pH} is the oxide thickness (in μm) for the high pH environment, y_{pw} is the oxide thickness (in μm) in pure water, and t is the time in days (note that this analysis differs slightly from that in [32]). The trend curves may be used to derive the rates, and the rate ratio may be used, via an Arrhenius expression, to derive an activation energy of 74.2kJ/mol for oxidation in this temperature range. This value is within the range of activation energies found for pretransition oxidation in different Zr alloys around this exposure temperature [48] [49] [50] [51] [52], indicating that any effect of pH or solute content on the oxidation rate was, indeed negligible.

Similarly, if the pure water points for the second cycle are shifted by Δt_{trans} , where Δt_{trans} is the difference in transition times (the difference between the red and green dashed lines in Figure 5), then the difference between second cycle oxidation rates in the two environments also appears to be dominated by the effect of temperature, not the availability of protons (or some undetermined solute effect). The change in the time to transition itself is also consistent with an effect of temperature [52].

Consistent with this (lack of an) effect of pH on the oxide, the effect of changing the environment on the relation between the suboxide thickness and the oxide thickness is indistinguishable from scatter both before and after transition. Transition, however, has a marked effect on the hydrogen pickup rate in the two environments, as shown in Figure 16. In most of the pretransition period, the hydrogen picked up is minimal, and similar in the two environments; close to transition, the hydrogen pickup rate increases in both, but becomes around five times higher in pure water than in the high pH environment [32]. This relation (or lack of a relation) between oxidation, pH and hydrogen pickup provides an insight into the nature of the species which carries hydrogen across the oxide into the metal substrate. The inward flux of O^{2-} anions which permits the oxide to grow must be balanced by an outward flux of electrons to avoid charge build-up. In a semi-conductor such as the ZrO_2 layer on Zircaloy-4, the mobile electron density and, hence, the flux is small, so a potential drop develops across the oxide until the fluxes can match. It is this combined diffusion, electromigration process, which produces time exponents less than $n=0.5$ for Zr alloys (sub-parabolic growth) [34]. The Zircaloy-4 alloy oxidises with an exponent, n , significantly less than 0.5, suggesting that the field across the oxide layer plays an important part in determining the oxidation rate. The higher hydrogen pickup rate in the lower pH environment might suggest that the mobile species for

hydrogen is a proton. If this were the case, however, then the increased flux of protons in the pure water environment in the second cycle would affect the field across the oxide which, in turn, would affect the oxidation rate. Since the oxidation rate is unaffected by the pH and solute content differences between the two environments, it appears more likely that the mobile species has no net charge. While the pH affects the rate of supply of protons to the oxide surface it seems that the protons must be discharged by electrons emerging from the oxide film to produce atomic hydrogen [5] before they can pass across the oxide.

More generally, the microstructural characteristics of the dioxide, the ZrO, the OSZ and (as shown in a companion paper) the oxidising SPPs are consistent as a function of pH and cycle, at least for the first and second cycles. Thus these characteristics must not affect, or be affected by, the hydrogen pickup rate. Further insight into the hydrogen pickup rate must come from the investigation of other features such as the fossil oxide-to- new oxide interface or from consideration of the behaviour of the bulk environment versus the constrained environment within the crack network.

6. Summary and Conclusions

Oxide growth and hydrogen pickup have been measured for Zircaloy-4 in environments of different pH. A detailed study of the metal-oxide interface has been carried out over sufficient lengths of interface to show meaningful trends in the behaviour of the ZrO and oxygen-saturated metal layers.

The distribution of both the ZrO and OSZ are influenced by the local metal and oxide orientation, but the average width of each is a constant fraction of the dioxide width prior to transition. The local variations are caused by kinetic effects. The observation that $n=0.3$ not only for the dioxide but also for the ZrO and OSZ is new and requires further investigation for the light it might shed on the mechanisms of oxidation and oxygen transfer between phases.

The suboxide width decreases rapidly at transition, then increases more slowly. The suboxide width as a proportion of the dioxide width also drops then increases after transition.

DFT shows that ZrO is less stable under tension, but is unlikely to be rendered generally unstable by the stresses developed within the undulations in the oxidation front.

The behaviour of the suboxide can be explained on the assumption that the dioxide layer is the protective layer until it is bypassed by the environment percolating into the crack network.

Hydrogen pickup is not affected by the choice of environments used here until close to transition. After transition the hydrogen pickup fraction is significantly greater in the lower-pH environment.

This is most likely to be due to the greater availability of protons in the lower-pH environment although the possibility of some other influence of the solutes cannot be neglected.

The hydrogen pickup rate affects neither the dioxide nor the suboxide growth rates. This absence of a correlation between the movement of hydrogen and that of oxygen across the oxide indicates that the hydrogen flux does not affect the potential drop across the oxide which, in turn, suggests that the hydrogen does not move as a consistently charged species.

Acknowledgements

JS, SLP and SO are grateful to the National Nuclear Laboratory and the EPSRC for funding this work. The EPSRC (EP/K040375/1 and EP/N010868/1) is acknowledged for funding the 'South of England Analytical Electron Microscope' and the FIB/SEM used in this research. The authors would like to thank Wood plc for the provision of autoclave facilities, CCFE for access to their TDS equipment, Westinghouse and PSI for their measurements of hydrogen content and Oxford University for the provision of all other laboratory facilities. We are also grateful to Colin English and the many members of the MUZIC-2 consortium for their insights, information and helpful discussions.

References

- [1] H. G. Rickover, L. D. Geiger and B. Lustman, "History of the development of zirconium alloys for use in nuclear reactors. Report TID-26740," US Energy Research And Development Administration, 1975.
- [2] D. O. Northwood, "The development and applications of zirconium alloys," *Materials & Design*, vol. 6, no. 2, pp. 58-70, 1985.
- [3] G. P. Sabol, "ZIRLO(TM) - An alloy development success," in *Zirconium In The Nuclear Industry: 14th Int. Symp. ASTM STP 1467*, West Conshohocken, PA, USA, 2005.
- [4] Z. Duan, H. Yang, Y. Satoh, K. Murakami, S. Kano, Z. Zhao, J. Shen and H. Abe, "Current status of materials development of nuclear fuel cladding tubes for light water reactors," *Nuclear Engineering & Design*, vol. 316, pp. 131-150, 2017.

- [5] B. Cox, V. G. Kritsky, C. Lemaignan, V. Polley, I. G. Ritchie, H. Ruhmann, V. N. Shishov, Y. K. Bibilashvili and A. V. Nikulina, "Waterside Corrosion Of Zirconium Alloys In Nuclear Power Plants. IAEA-TECDOC-996," IAEA, Vienna, 1993.
- [6] B. Cox, "Some thoughts on the mechanisms of in-reactor corrosion of zirconium alloys," *J. Nuclear Mater.*, vol. 336, pp. 331-368, 2005.
- [7] J. S. Bryner, "Cyclic nature of corrosion of Zircaloy-4 in 633K water," *J. Nuclear Mater.*, vol. 82, pp. 84-101, 1979.
- [8] A. J. G. Maroto, R. Bordoni, M. Villegas, A. M. Olmedo, M. A. Blesau, A. Iglesias and P. Koenig, "Growth and characterization of oxide layers on zirconium alloys," *J. Nuclear Mater.*, vol. 229, pp. 79-92, 1996.
- [9] A. T. Motta, A. Yilmazbayhan, R. J. Comstock, J. Partezana, G. P. Sabol, B. Lai and Z. Cai, "Microstructure and growth mechanism of oxide layers formed on Zr alloys studied with microbeam synchrotron radiation," *J. ASTM Intl.*, vol. 2, no. 5, p. JAI 12375, 2005.
- [10] J.-Y. Park, S.-J. Yoo, B.-K. Choi and Y. H. Jeong, "Oxide microstructures of advanced Zr alloys corroded in 360°C water loop," *J. Alloys & Compounds*, vol. 437, pp. 274-279, 2007.
- [11] A. Yilmazbayhan, E. Breval, A. T. Motta and R. J. Comstock, "Transmission electron microscope examination of oxide layers formed on Zr alloys," *J. Nuclear Mater.*, vol. 349, pp. 265-281, 2006.
- [12] P. Bossis, G. Lelievre, P. Barberis, X. Iltis, F. Lefebvre, L. Thomas and M. Maguire, "Multi-scale characterization of the metal-oxide interface of zirconium alloys," in *Zirconium In The Nuclear Industry: Twelfth Int. Symp. ASTM STP 1354*, G. P. Sabol and G. D. Moan, Eds., Toronto, Canada, ASTM, 2000, pp. 918-945.
- [13] N. Ni, S. Lozano-Perez, J. M. Sykes, G. D. W. Smith and C. R. M. Grovenor, "Focussed ion beam sectioning for the 3D characterisation of cracking in oxide scales formed on commercial ZIRLO(TM) alloys during corrosion in high temperature pressurised water," *Corr. Sci.*, vol. 53, pp. 4073-4083, 2011.
- [14] N. Ni, S. Lozano-Perez, M. L. Jenkins, G. D. W. Smith, J. M. Sykes and C. R. M. Grovenor, "Porosity in oxides on zirconium fuel cladding alloys, and its importance in controlling oxidation rates," *Scripta Mater.*, vol. 62, pp. 564-567, 2010.
- [15] S. Ortner, H. Swan, A. Laferrere, C. English, J. Hyde, P. Styman, K. Jurkschat, H. Hulme, A. Pantelli, M. Gass, V. Allen and P. Frankel, "Study of Zircaloy corrosion to develop mechanistic

understanding," in *Fontevraud 8 - Contribution Of Materials Investigations And Operating Experience To LWR Safety, Performance And Reliability*, Avignon, France, 2014.

- [16] P. Bossis, F. Lefebvre, P. Barberis and A. Galerie, "Corrosion of zirconium alloys: Link between the metal/oxide roughness, the degradation of the protective oxide layer and the corrosion kinetics," *Mater. Sci. Forum*, Vols. 369-372, pp. 255-262, 2001.
- [17] P. Platt, S. Wedge, P. Frankel, M. Gass, R. Howells and M. Preuss, "A study into the impact of interface roughness development on mechanical degradation of oxides formed on zirconium alloys," *J. Nuclear Mater.*, vol. 459, pp. 166-174, 2015.
- [18] H. Swan, M. S. Blackmur, J. M. Hyde, A. LaFerrere, S. R. Ortner, P. D. Styman, C. Staines, M. Gass, H. Hulme, A. Cole-Baker and P. Frankel, "The measurement of stress and phase fraction distributions in pre and post-transition Zircaloy oxides using nano-beam synchrotron X-ray diffraction," *J. Nuclear Mater.*, vol. 479, pp. 559-575, 2016.
- [19] B. Holmberg and T. Dagerhamn, "X-Ray studies on solid solutions of oxygen in α -zirconium," *Acta Chimica Scandinavica*, vol. 15, pp. 919-925, 1961.
- [20] C. Morant, J. M. Sanz, L. Galan, L. Soriano and F. Rueda, "An XPS study of the interaction of oxygen with zirconium," *Surf. Sci.*, vol. 218, pp. 331-345, 1989.
- [21] G. R. Corallo, D. A. Asbury, R. E. Gilbert and G. B. Hoflund, "Electron-energy loss study of clean and oxygen-exposed polycrystalline zirconium," *Phys. Rev. B*, vol. 35, no. 18, pp. 9451-9459, 1987.
- [22] B. de Gabory, Y. Dong, A. T. Motta and E. A. Marquis, "EELS and atom probe tomography study of the evolution of the metal/oxide interface during zirconium alloy oxidation," *J. Nuclear Mater.*, vol. 462, pp. 304-309, 2015.
- [23] Y. Dong, A. T. Motta and E. A. Marquis, "Atom probe tomography study of alloying element distributions in Zr alloys and their oxides," *J. Nuclear Mater.*, vol. 442, no. 1-3, pp. 270-281, 2013.
- [24] N. Ni, D. Hudson, J. Wei, P. Wang, S. Lozano-Perez, G. D. W. Smith, J. M. Sykes, S. S. Yardley, K. L. Moore, S. Lyon, R. Cottis, M. Preuss and C. R. M. Grovenor, "How the crystallography and nanoscale chemistry of the metal/oxide interface develops during the aqueous oxidation of zirconium cladding alloys," *Acta Mater.*, vol. 60, pp. 7132-7149, 2012.

- [25] E. Marquis, J. Hyde, D. W. Saxey, S. Lozano-Perez, V. de Castro, D. Hudson, C. A. Williams, S. Humphry-Baker and G. D. W. Smith, "Nuclear reactor materials at the atomic scale," *Mater. Today*, vol. 12, no. 11, pp. 30-37, 2009.
- [26] N. Ni, S. Lozano-Perez, J. Sykes and C. Grovenor, "Quantitative EELS analysis of zirconium alloy metal/oxide interfaces," *Ultramic.*, vol. 111, pp. 123-130, 2011.
- [27] J. Hu, B. Setiadinata, T. Aarholt, A. Garner, A. Vilalta-Clemente, J. Partezana, P. Frankel, P. Bagot, S. Lozano-Perez, A. Wilkinson, M. Preuss, M. Moody and C. Grovenor, "Understanding corrosion and hydrogen pickup of zirconium fuel cladding alloys: The role of oxide microstructure, porosity, suboxides and second phase particles," in *Zirconium In The Nuclear Industry: 18th Int. Symp. ASTM STP 1597*, R. J. Comstock and A. T. Motta, Eds., West Conshohocken, PA, USA, ASTM, 2018, pp. 93-126.
- [28] J. Hu, A. Garner, N. Ni, A. Gholinia, R. J. Nicholls, S. Lozano-Perez, P. Frankel, M. Preuss and C. R. M. Grovenor, "Identifying suboxide grains at the metal-oxide interface of a corroded 1.0%Nb alloy using (S)TEM, transmission-EBSD and EELS," *Micron*, vol. 69, pp. 35-42, 2015.
- [29] A. T. Motta, A. Yilmazbayhan, M. J. G. da Silva, R. J. Comstock, G. S. Was, J. T. Busby, E. Gartner, Q. Peng, Y. H. Jeong and J. Y. Park, "Zirconium alloys for supercritical water reactor applications: Challenges and possibilities," *J. Nuclear Mater.*, vol. 371, pp. 61-75, 2007.
- [30] X. Iltis and H. Michel, "Transmission electron microscopy study of a locally ordered Zr-O solid solution obtained by and oxidation treatments of a Zircaloy-4 alloy," *J. Alloys Compounds*, vol. 177, no. 5, pp. 71-82, 1991.
- [31] T. Ericsson, G. Ostberg and B. Lehtinen, "Some observations on Zr-O solid solutions with a microprobe and by electron microscopy," *J. Nuclear Mater.*, vol. 25, pp. 322-327, 1968.
- [32] J. Sayers, S. Ortner, K. Li and S. Lozano-Perez, "Effect of pH on hydrogen pick-up and corrosion in Zircaloy-4," in *Proc. 18th Int. Conf. on Environmental Degradation Of Materials In Nuclear Power Systems - Water Reactors*, 2017.
- [33] H. Coriou, L. Grall, J. Meunier, M. Plras and H. Willermoz, "Corrosion du Zircaloy dans divers milieux alcalins a haute temperature," *J. Nuclear Mater.*, vol. 7, no. 3, pp. 320-327, 1962.
- [34] A. Couet, A. T. Motta and A. Ambard, "The coupled current charge compensation model for zirconium alloy fuel cladding oxidation: I. Parabolic oxidation of zirconium alloys," *Corr. Sci.*, vol. 100, pp. 73-84, 2015.

- [35] J. Sayers, *Effect Of pH On Hydrogen Pickup And Corrosion Of Zircaloy-4*, University Of Oxford, 2017.
- [36] J. Mayer, L. A. Gianuzzi, T. Kamino and J. Michael, "TEM sample preparation and damage," *MRS Bulletin*, vol. 32, pp. 400-407, 2007.
- [37] N. Ni, *Study of oxidation mechanisms of zirconium alloys by electron microscopy*, United Kingdom: Oxford University, 2011.
- [38] S. Lozano-Perez, "A guide on FIB preparation of samples containing stress corrosion crack tips for TEM and atom probe analysis," *Micron*, vol. 39, no. 3, pp. 320-328, 2008.
- [39] K. M. I. M. Annand, "Utilising DualEELS to probe the nanoscale mechanisms of the corrosion of Zircaloy-4 in 350 °C pressurised water," *Journal of Nuclear Materials*, vol. 465, pp. 390-399, 2015.
- [40] P. Longo, "The use of MLLS fitting approach to resolve overlapping edges in the EELS spectrum at the atomic level," [Online]. Available: <http://gatan.com/use-mls-fitting-approach-resolve-overlapping-edges-eels-spectrum-atomic-level>.
- [41] S. Clark, M. Segall, C. Pickard, H. P.J., M. Probert, K. Refson and M. Payne, "First principles methods using CASTEP," *Zeitschrift fuer Kristallographie*, pp. 567-570, 2005.
- [42] A. Couet, A. T. Motta and R. J. Comstock, "Hydrogen pickup measurements in zirconium alloys: Relation to oxidation kinetics," *Journal of Nuclear Materials*, vol. 451, no. 1-3, pp. 1-13, 2014.
- [43] B. Ensor, A. M. Lucente, M. J. Frederick, J. Sutliff and A. T. Motta, "The role of hydrogen in zirconium alloy corrosion," *Journal of Nuclear Materials*, vol. 496, pp. 301-312, 2017.
- [44] G. Sundell, M. Thuvander and H.-O. Andren, "Barrier oxide chemistry and hydrogen pick-up mechanisms in zirconium alloys," *Corr. Sci.*, vol. 102, pp. 490-502, 2016.
- [45] M. Parise, O. Sicardy and G. Cailletaud, "Modelling of the mechanical behavior of the metal-oxide system during Zr alloy oxidation," *J. Nuclear Mater.*, vol. 256, pp. 35-46, 1998.
- [46] S. Ortner, M. Blackmur, M. Fenwick and H. G. M. Weekes, "The role of metal plasticity in the growth of oxide on Zircaloy-4," in *Fontevraud 9: Contribution of Materials Investigations and Operating Experience to Light Water NPPs' Safety Performance and Reliability*, Avignon, France, 2018.

- [47] T. Kido, S. Wada, T. Takahashi, H. Uchida, I. Komine and Y. Inoue, "Behavior of Lithium and Boron in irradiated and unirradiated oxides formed on Zircaloy-4 claddings," in *Zirconium in the Nuclear Industry: Twelfth International Symposium*, West Conshohocken, PA, 2001.
- [48] L. Castaldelli, C. Fizzotti and L. Lunde, "Long-term test results of promising new zirconium alloys," in *Zirconium in the Nuclear Industry: Fifth Conference. ASTM STP 754*, Boston, USA, 1982.
- [49] H. R. Peters, "Improved characterization of aqueous corrosion kinetics of Zircaloy-4," in *Zirconium in the Nuclear Industry: Sixth Int. Symp. ASTM STP 824*, Vancouver, Canada, 1984.
- [50] P. Billot, P. Beslu, A. Giordano and J. Thomazet, "Development of a mechanistic model to assess the external corrosion of the Zircaloy claddings in PWRs," in *Zirconium in the Nuclear Industry: Eighth Int. Symp. ASTM STP 1023*, San Diego, USA, 1989.
- [51] R. A. Perkins and R. A. Busch, "Corrosion of Zircaloy in the presence of LiOH," in *Zirconium in the Nuclear Industry: Ninth Int. Symp. ASTM STP 1132*, Kobe, Japan, 1991.
- [52] E. Hillner, "Corrosion of Zirconium-Base Alloys—An Overview," in *Zirconium in the Nuclear Industry*, West Conshohocken, PA, 1977.

Figure captions

Figure 20 – HAADF image showing the oxide-metal interface region on sample exposed to $\text{pH}_{350}=8.82$ for 91 days ($1.83\mu\text{m}$). The numbers indicate the location of the extracted reference spectra in Figure 2. The labelled regions are: 1 – Metal, 2 – Hydride, 3 – SPP (one in the oxide and one in the metal), 4 – Oxygen Saturated Zirconium (OSZ), 5 – ZrO, 6 – Oxide. The box shows the size of the area used to extract the reference spectra ($\sim 100\times 100\text{nm}$)

Figure 21 – EELS spectra showing the plasmon peaks for the different regions labelled in Figure 1.

Figure 22 – MLLS fit for the 6 regions in Figure 1 From top to bottom: Metal, Hydrides, SPPs, OSZ, ZrO, and Oxide. Lighter areas show the strongest match to the input spectrum.

Figure 23 – Segmented OSZ map (now a binary image)

Figure 24 - Comparison of samples oxidized in pure water at 360°C vs samples oxidized in elevated pH at 350°C .

Figure 25 - OSZ map at OM interface in a sample exposed 15 days to high pH water (oxide thickness = $0.96\mu\text{m}$)

Figure 26 - ZrO map in region shown in Figure 6.

Figure 27 - OSZ map at OM interface in a sample exposed 27 days to high-pH water.

Figure 28 - ZrO map in region shown in Figure 8 .

Figure 29 – (Top) OSZ map at OM interface in a sample exposed 62 days to high-pH water. (Bottom) ZrO map. The white arrow indicates a region of ZrO separated from the rest of the ZrO + OSZ region.

Figure 30 – (Top) OSZ map at OM interface of sample exposed 123 days in high-pH water. (Bottom) ZrO map.

Figure 31 – (Top) OSZ maps at OM interface of sample exposed 148 days to high-pH water. (Bottom) ZrO map

Figure 32 – (Top) OSZ maps at OM interface of sample exposed 211 days to high-pH water. (Bottom) ZrO maps

Figure 33 - Variation in the thicknesses of the OSZ + ZrO regions during oxidation in high pH water at 360°C and in pure water at 350°C . The error bars are the standard deviation of the data.

Figure 34 – Different intermediate layers as proportions of oxide thickness. (a) Ratio of ZrO and OSZ to ZrO_2 thickness in high pH. (b) Ratio of $\text{ZrO}+\text{OSZ}$ to ZrO_2

Figure 35. Comparison of hydrogen content (H_2) for samples oxidised in pure water and the combined $\text{H}_2 + \text{DH} + \text{D}_2$ for samples oxidised in a high pH (50% deuterated), against oxide thickness

Figure 36. Variation in the formation enthalpy of the different phases with hydrostatic pressure.

Figure 37. Convex hull for 0 GPa and the position of the formation enthalpy of ZrO

Figure 38. Position of interfaces of oxide and suboxide, width of suboxide layer and ratio of suboxide width to oxide thickness when both interfaces move according to $\text{distance}=\text{At}^n$ with $A_{\text{suboxide}}=1.1*A_{\text{oxide}}$, $n=0.3$, and the effective oxide thickness falls to zero at transition (arbitrary units for the purpose of qualitative comparison).